

# Resolution analysis of geophysical images: Comparison between point spread function and region of data influence measures

Carlyle R. Miller\* and Partha S. Routh

Dept. of Geosciences, Boise State University, 1910 University Drive, Boise, ID 83725-1535, USA

Received June 2006, revision accepted September 2006

## ABSTRACT

Practical decisions are often made based on the subsurface images obtained by inverting geophysical data. Therefore it is important to understand the resolution of the image, which is a function of several factors, including the underlying geophysical experiment, noise in the data, prior information and the ability to model the physics appropriately. An important step towards interpreting the image is to quantify how much of the solution is required to satisfy the data observations and how much exists solely due to the prior information used to stabilize the solution. A procedure to identify the regions that are not constrained by the data would help when interpreting the image. For linear inverse problems this procedure is well established, but for non-linear problems the procedure is more complicated. In this paper we compare two different approaches to resolution analysis of geophysical images: the region of data influence index and a resolution spread computed using point spread functions. The region of data influence method is a fully non-linear approach, while the point spread function analysis is a linearized approach. An approximate relationship between the region of data influence and the resolution matrix is derived, which suggests that the region of data influence is connected with the rows of the resolution matrix. The point-spread-function spread measure is connected with the columns of the resolution matrix, and therefore the point-spread-function spread and the region of data influence are fundamentally different resolution measures. From a practical point of view, if two different approaches indicate similar interpretations on post-inversion images, the confidence in the interpretation is enhanced. We demonstrate the use of the two approaches on a linear synthetic example and a non-linear synthetic example, and apply them to a non-linear electromagnetic field data example.

## INTRODUCTION

Geophysical inversion is inherently ill-posed and non-unique. To solve ill-posed geophysical inverse problems, we routinely incorporate prior information into our solution. This stabilizes the solution, but also complicates the appraisal process because of the bias introduced into the solution. If the end goal of our data analysis involves decisions based on our solution, it is of great importance that we take steps to quantify how

much information came from data and how much came from prior information.

For different applications it is difficult to produce a unified interpretation goal; however, an important question is to determine which regions of the image are influenced by *a priori* information and which regions are influenced by the data. Although different ways of incorporating *a priori* information are sometimes considered to be subjective (Friedel 2003), regularization an essential step in obtaining a stable solution that is physically meaningful. Therefore, we usually cannot neglect imposing *a priori* information through the regularization procedure in the inverse problem. However, if we can

---

\*E-mail: camiller@cgiss.boisestate.edu

develop some procedure to separate out the regions that are not constrained by the data, then it would greatly simplify the interpretation and provide a robust way of connecting the interpretation with the physical experiment that generated the data. Oldenburg and Li (1999) used two reference models in a non-linear DC resistivity inversion to determine the regions that are honoured by the data and generate a filter function called depth-of-investigation curves to interpret the inverted image. Alumbaugh and Newman (2000) used 50% spread criteria from the point spread functions to highlight the regions of the model that are better resolved. In seismic tomography, some commonly applied approaches with a similar goal are the impulse test and the checkerboard test. In these approaches, the raypaths of the real data are used on a synthetic impulse model or checkerboard model to generate the data. Subsequently, the inverted images are compared with the synthetic model in order to understand the model resolution (Shearer 1999).

In the depth-of-investigation approach of Oldenburg and Li (1999), the index is computed using the models obtained from two inversion runs with different reference models. The image region that is most influenced by the data has a low depth-of-investigation index and we refer to this region as the region of data influence. The advantage of this approach is that it can be applied to non-linear problems without any linearization assumption. Alternatively, the resolving capability of the geophysical data can be obtained by computing columns of the resolution matrix, called point spread functions. We examine spread measures computed using point spread functions and compare them with the region of data influence index. Both of these methods have previously been used in the context of appraisal analysis (Oldenburg and Li 1999; Alumbaugh and Newman 2000). Oldenborger (2006) applied the region of data influence approach to the 3D electrical-resistivity-tomography experiment and showed that it is a better approach to examining resolution, compared to sensitivity measures.

In this paper, we show the similarity of the two approaches. From a practical point of view, if two different approaches indicate similar interpretations on post-inversion images, the confidence in the interpretation is enhanced. The examples presented in this paper are one-dimensional (1D). We recognize that in reality the earth is three-dimensional (3D), but the generic procedure of the approaches presented here will be valid for problems in any dimensions. For computational ease, we use 1D examples throughout the paper. The paper is presented as follows: Using a linear problem we examine the relationship and the mathematical connections that exist

between the two appraisal tools. We illustrate the relationship with a linear synthetic example and a non-linear synthetic example, and we apply it to a non-linear field example using controlled source electromagnetics.

## RESOLUTION MEASURES

### Linearized resolution analysis

Insight into the resolution analysis problem can be gained by considering a linear inverse problem,  $\mathbf{d}^{\text{obs}} = \mathbf{G}\mathbf{m} + \varepsilon$ . The linear problem has been studied in detail in previous literature (Backus and Gilbert 1968, 1970; Oldenburg 1983; Snieder 1990; Parker 1994; Alumbaugh and Newman 2000) and here we present the necessary equations to illustrate the various components of the resolution measure. In a linear problem, the objective function to be minimized is

$$\phi = \left\| \mathbf{W}_d(\mathbf{d}^{\text{obs}} - \mathbf{G}\mathbf{m}) \right\|^2 + \beta \left\| \mathbf{W}_m(\mathbf{m} - \mathbf{m}_0) \right\|^2, \quad (1)$$

where  $\mathbf{G} \in \mathbb{R}^{N \times M}$  is forward modelling operator,  $\mathbf{W}_d \in \mathbb{R}^{N \times N}$  is the data weighting matrix,  $\mathbf{W}_m \in \mathbb{R}^{M \times M}$  is the model weighting matrix used to impose constraints in the solution such as smoothing,  $\mathbf{m} \in \mathbb{R}^{M \times 1}$  is the model vector,  $\mathbf{m}_0 \in \mathbb{R}^{M \times 1}$  is the reference model vector,  $\mathbf{d}^{\text{obs}} \in \mathbb{R}^{N \times 1}$  is the data vector and  $\beta$  is the regularization parameter that controls the relative contribution of the data misfit and the model norm. Denoting the Hessian by  $\mathbf{H} = (\mathbf{G}^T \mathbf{W}_d^T \mathbf{W}_d \mathbf{G} + \beta \mathbf{W}_m^T \mathbf{W}_m)$ , the recovered model is given by

$$\hat{\mathbf{m}} = \mathbf{H}^{-1} \mathbf{G}^T \mathbf{W}_d^T \mathbf{W}_d \mathbf{G} \mathbf{m} + \mathbf{H}^{-1} \mathbf{G}^T \mathbf{W}_d^T \mathbf{W}_d \varepsilon + \mathbf{H}^{-1} \mathbf{W}_m^T \mathbf{W}_m \mathbf{m}_0. \quad (2)$$

In a more compact notation we can represent the estimated model in equation (2) by  $\hat{\mathbf{m}} = \mathbf{R}\mathbf{m} + \eta + \gamma$ , where  $\mathbf{R}$  is the resolution matrix,

$$\mathbf{R} = (\mathbf{G}^T \mathbf{W}_d^T \mathbf{W}_d \mathbf{G} + \beta \mathbf{W}_m^T \mathbf{W}_m)^{-1} \mathbf{G}^T \mathbf{W}_d^T \mathbf{W}_d \mathbf{G}. \quad (3)$$

$\mathbf{R}$  provides a linear mapping between the estimated model parameters,  $\hat{\mathbf{m}}$  and the true model parameters,  $\mathbf{m}$ . For a non-linear problem given by  $\mathbf{d}^{\text{obs}} = F(\mathbf{m}) + \varepsilon$ , the estimated solution for the model perturbation is given by

$$\delta \hat{\mathbf{m}} = \mathbf{H}^{-1} \mathbf{G}^T \mathbf{W}_d^T \mathbf{W}_d \mathbf{G} \delta \mathbf{m} + \mathbf{H}^{-1} \mathbf{G}^T \mathbf{W}_d^T \mathbf{W}_d (Q(\delta \mathbf{m}) - P(\delta \hat{\mathbf{m}}) + \varepsilon) + \mathbf{H}^{-1} \mathbf{W}_m^T \mathbf{W}_m \delta \mathbf{m}_0, \quad (4)$$

where  $\mathbf{G}$  is the sensitivity matrix,  $\delta \mathbf{m} = \mathbf{m}^{(k+1)} - \mathbf{m}^{(k)}$  is the model perturbation,  $\delta \mathbf{m}_0 = \mathbf{m}_0 - \mathbf{m}^{(k)}$  is difference between the reference model and the model estimate at the  $k$ th iteration and  $Q(\delta \mathbf{m})$ ,  $P(\delta \hat{\mathbf{m}})$  are the higher-order terms, typically neglected in the linearized analysis. When the higher-order

terms are not negligible, bias is introduced into the solution of the estimated model, in addition to the bias introduced by the reference model. For our analysis we will neglect the higher-order terms and carry out the interpretation using linearized analysis, using  $\mathbf{R}$  in equation (3) as resolution mapping.

### Point spread functions

The columns of the resolution matrix are called the point spread functions. A point spread function describes how a delta-like perturbation in the model manifests itself in the inverted result. If a particular point spread function is wide and/or has large side lobes, then the corresponding model is poorly resolved at that location and the resolution ‘width’ is broader than the cell dimension. This introduces the idea that spread of these point spread functions can be used as a measure to assess the resolving capability of the data and the prior information. We note that the prior information can effectively be treated as data in the inverse problem, so the point spread function and hence the spread will be influenced by the prior information.

### Spread criterion for the point spread function

To compare the resolution capability of the data and prior information in different regions of the model, point spread functions can be compared directly with each other. This can be useful especially in large-scale problems where the question about resolvability is limited to few specific regions of the model. Although the point spread function comparison is a valid procedure and has the capability to convey a significant amount of detail, the process can be tedious when we are faced with comparing thousands of cells throughout the entire model instead of a few cells within a specific region of interest. Here, we develop a spread criterion to summarize the information contained in the point spread function to a single number.

In general, there are many possibilities when choosing the spread criterion, i.e. spread definition is non-unique. The idea is very similar to the definition of attributes computed from time–frequency maps (Barnes 1993; Sinha *et al.* 2005). For each cell, this number can be used as a diagnostic measure to compare the resolving capability of the inverse operator in different regions of the model. We propose the following definition of the spread (Routh and Miller 2006):

$$S(\mathbf{r}_k) = \left[ \frac{\int \mathbf{W}(\mathbf{r}, \mathbf{r}_k) (p(\mathbf{r}, \mathbf{r}_k) - \Delta(\mathbf{r}, \mathbf{r}_k))^2 d\mathbf{r}}{\alpha + \int p^2(\mathbf{r}, \mathbf{r}_k) d\mathbf{r}} \right]^{1/2}, \quad (5)$$

where  $\mathbf{W}(\mathbf{r}, \mathbf{r}_k)$  is a distance weighting matrix that increases the spread value when side lobes exist away from the region of interest. We choose the weighting matrix as  $\mathbf{W}(\mathbf{r}, \mathbf{r}_k) = 1 + |\mathbf{r} - \mathbf{r}_k|^\lambda$  where  $\lambda \geq 1$ . For our examples we choose  $\lambda = 1$ , and  $\Delta(\mathbf{r}, \mathbf{r}_k) = 1$  when  $\mathbf{r} = \mathbf{r}_k$  and  $\Delta(\mathbf{r}, \mathbf{r}_k) = 0$  for  $\mathbf{r} \neq \mathbf{r}_k$ . The point spread function  $p(\mathbf{r}, \mathbf{r}_k)$  is for the cell whose centre is at  $\mathbf{r}_k$ , and  $\alpha$  is a small threshold parameter chosen so that the denominator in the spread equation is not equal to zero when the energy of the point spread function is zero. This can occur in regions of insufficient data coverage. If the point spread function peak is shifted from the region of interest, the chosen spread criterion will generate large spread values. In subsequent sections we demonstrate the use of the point spread function and spread criterion to interpret inverted models obtained from a synthetic linear inverse problem, a synthetic non-linear inverse problem and a field example with frequency-domain controlled-source electromagnetic data.

### Averaging kernels

The rows of the resolution matrix are the averaging or Backus–Gilbert kernels (Backus and Gilbert 1970). These kernels show how the value of a specific model parameter is obtained by averaging the model in the entire domain. If the averaging kernel is a delta-like function at a certain location, then the contribution to the estimated value is obtained from that region and the contribution to the average value from other regions of the model is insignificant. If we remove the effect of the reference model in equation (2) from the inversion then the average value of the model parameter can be represented by the following equation:

$$\langle \hat{\mathbf{m}} \rangle = \hat{\mathbf{m}} - \mathbf{H}^{-1} \mathbf{W}_m^T \mathbf{W}_m \mathbf{m}_0 = \mathbf{R} \mathbf{m} + \boldsymbol{\eta}. \quad (6)$$

The average value of the model parameter is equal to the projection of the Backus–Gilbert averaging kernel (i.e. row of  $\mathbf{R}$ ) on to the true model plus the noise contribution. The average value is obtained by subtracting the bias due to the reference model as shown in equation (6). Since  $\langle \hat{\mathbf{m}} \rangle_k$  is obtained by projecting the averaging kernel on the true model, we denote it as the average value of the model estimate. Thus three quantities: the average value  $\langle \hat{\mathbf{m}} \rangle_k$ , the averaging kernel  $\mathbf{r}^k = \mathbf{R}(k, :)$  and the noise contribution  $\boldsymbol{\eta}_k$ , should be jointly interpreted. The uncertainty of the average value of a specific model parameter is associated with the noise contribution and the spread of the averaging kernel. We note that the point spread functions, which are more informative about the inverse operator, are fundamentally different from Backus–Gilbert kernels and we demonstrate this difference using a linear example.

### Region of data influence

For the regularized solution given by equation (2), in regions unconstrained by the data, the estimated model will revert to the reference model. This is the fundamental idea behind the depth-of-investigation index introduced by Oldenburg and Li (1999). Thus, by inverting the same data (with the same noise assumption) using two different reference models, a region of data influence (RDI) can be constructed as proposed by Oldenburg and Li (1999):

$$RDI = \frac{|\hat{\mathbf{m}}_2 - \hat{\mathbf{m}}_1|}{|\mathbf{m}_2^{\text{ref}} - \mathbf{m}_1^{\text{ref}}|}. \quad (7)$$

In regions of the model that are unconstrained by the data, this ratio will go to unity, whereas in the regions constrained by the data, this ratio will approach zero. In subsequent sections, we construct this resolution measure for three examples by calculating this ratio over the entire model domain. In theory, the reference model can be a heterogeneous or a homogeneous model; however, in most cases a homogeneous reference model is used (Oldenburg and Li 1999). The advantage of the region of data influence measure is it does not depend on the linearization assumption for non-linear problems. However, for linearized iterative algorithms, the reference models cannot be far from the true reference model, due to convergence problems.

### RELATIONSHIP BETWEEN THE RESOLUTION MATRIX AND RDI

In this section we examine the connection between the resolution matrix and the region of data influence function. We examine the relationship using a linear inverse problem since the mathematical operations are simpler. The estimated model in equation (2) can be written in an alternative form, given by

$$\hat{\mathbf{m}} = \mathbf{m}_0 + \mathbf{R}(\mathbf{m} - \mathbf{m}_0) + \mathbf{H}^{-1} \mathbf{G}^T \mathbf{W}_d^T \mathbf{W}_d \boldsymbol{\varepsilon}. \quad (8)$$

In the region of data influence approach, we use two different model estimates  $\hat{\mathbf{m}}_2, \hat{\mathbf{m}}_1$  for the corresponding reference models  $\mathbf{m}_0^2, \mathbf{m}_0^1$ . The difference between the estimates can be represented by

$$\hat{\mathbf{m}}_2 - \hat{\mathbf{m}}_1 = (\mathbf{m}_0^2 - \mathbf{m}_0^1) + \mathbf{R}_2(\mathbf{m} - \mathbf{m}_0^2) - \mathbf{R}_1(\mathbf{m} - \mathbf{m}_0^1) + [\mathbf{H}_2^{-1} - \mathbf{H}_1^{-1}] \mathbf{G}^T \mathbf{W}_d^T \mathbf{W}_d \boldsymbol{\varepsilon}, \quad (9)$$

where  $\mathbf{R}_2$  and  $\mathbf{R}_1$  are the resolution matrices obtained by inverting the data using the respective reference models  $\mathbf{m}_0^2, \mathbf{m}_0^1$ .

The  $k$ th element of the model difference is

$$(\hat{\mathbf{m}}_2 - \hat{\mathbf{m}}_1)_k = (\mathbf{m}_0^2 - \mathbf{m}_0^1)_k + (\mathbf{r}_2^k)^T (\mathbf{m} - \mathbf{m}_0^2) - (\mathbf{r}_1^k)^T (\mathbf{m} - \mathbf{m}_0^1) + [(\mathbf{h}_2^k)^T - (\mathbf{h}_1^k)^T] \mathbf{G}^T \mathbf{W}_d^T \mathbf{W}_d \boldsymbol{\varepsilon}, \quad (10)$$

where  $\mathbf{r}_2^k, \mathbf{r}_1^k$  are the averaging kernels, i.e. the  $k$ th row of the resolution matrix  $\mathbf{R}$ , and  $\mathbf{h}_2^k, \mathbf{h}_1^k$  are the  $k$ th row of the inverse Hessian matrices,  $\mathbf{H}_1^{-1} = \mathbf{H}^{-1}(\beta_1)$  and  $\mathbf{H}_2^{-1} = \mathbf{H}^{-1}(\beta_2)$ , respectively.

To analyze equation (9) or equation (10), we consider a simplified case where the model weighting matrix is only composed of the smallest component, i.e. there are no smoothing or flatness terms and therefore  $\mathbf{W}_m$  is a diagonal matrix. For computational ease, we simply consider the case where weighting is uniform and we use the identity matrix for model weighting. With this simplification, the resolution matrix in equation (3) can be written as  $\mathbf{R} = (\tilde{\mathbf{G}}^T \tilde{\mathbf{G}} + \beta \mathbf{I})^{-1} \tilde{\mathbf{G}}^T \tilde{\mathbf{G}}$ , where  $\tilde{\mathbf{G}} = \mathbf{W}_d \mathbf{G}$ . Thus for two different reference models, the difference in the resolution matrix is in the regularization term, i.e.  $\mathbf{R}_1 = \mathbf{R}(\beta_1) = (\tilde{\mathbf{G}}^T \tilde{\mathbf{G}} + \beta_1 \mathbf{I})^{-1} \tilde{\mathbf{G}}^T \tilde{\mathbf{G}}$  and  $\mathbf{R}_2 = \mathbf{R}(\beta_2) = (\tilde{\mathbf{G}}^T \tilde{\mathbf{G}} + \beta_2 \mathbf{I})^{-1} \tilde{\mathbf{G}}^T \tilde{\mathbf{G}}$ . Representing  $\tilde{\boldsymbol{\varepsilon}} = \mathbf{W}_d \boldsymbol{\varepsilon}$ , equation (9) can be written as

$$\hat{\mathbf{m}}_2 - \hat{\mathbf{m}}_1 = (\mathbf{m}_0^2 - \mathbf{m}_0^1) + (\mathbf{R}_2 - \mathbf{R}_1) \mathbf{m} - (\mathbf{R}_2 \mathbf{m}_0^2 - \mathbf{R}_1 \mathbf{m}_0^1) + [\mathbf{H}_2^{-1} - \mathbf{H}_1^{-1}] \tilde{\mathbf{G}}^T \tilde{\boldsymbol{\varepsilon}} \quad (11)$$

Equation (11) shows the mathematical connection between the region of data influence and the resolution matrices. Some insight can be gained by examining each term in equation (11) in detail. We use singular value decomposition (SVD) to analyze equation (11). Decomposing  $\tilde{\mathbf{G}} = \mathbf{U} \mathbf{\Lambda} \mathbf{V}^T$  using SVD, equation (11) can be written as (see Appendix A)

$$\hat{\mathbf{m}}_2 - \hat{\mathbf{m}}_1 = (\mathbf{m}_0^2 - \mathbf{m}_0^1) + \mathbf{V} \left( \frac{\Lambda^2}{\Lambda^2 + \beta_2} - \frac{\Lambda^2}{\Lambda^2 + \beta_1} \right) \mathbf{V}^T \mathbf{m} - \mathbf{V} \left( \frac{\Lambda^2}{\Lambda^2 + \beta_2} \mathbf{V}^T \mathbf{m}_0^2 - \frac{\Lambda^2}{\Lambda^2 + \beta_1} \mathbf{V}^T \mathbf{m}_0^1 \right) + \mathbf{V} \left( \frac{\Lambda}{\Lambda^2 + \beta_2} - \frac{\Lambda}{\Lambda^2 + \beta_1} \right) \mathbf{U}^T \tilde{\boldsymbol{\varepsilon}}. \quad (12)$$

### Analysis of the noise term $[\mathbf{H}^{-1}(\beta_2) - \mathbf{H}^{-1}(\beta_1)] \tilde{\mathbf{G}}^T \tilde{\boldsymbol{\varepsilon}}$

This term is the contribution of the noise on the recovered model parameters. Physically  $\tilde{\mathbf{G}}^T \tilde{\boldsymbol{\varepsilon}}$  is the projection of the noise on to the model space and the pre-multiplication by the inverse Hessian provides a scaling. The goal in this analysis is to see how this term contributes to the region of data influence

measure. The SVD representation of this term from equation (12) is given by

$$[\mathbf{H}^{-1}(\beta_2) - \mathbf{H}^{-1}(\beta_1)] \tilde{\mathbf{G}}^T \tilde{\boldsymbol{\varepsilon}} = \mathbf{V} \left( \frac{\Lambda}{\Lambda^2 + \beta_2} - \frac{\Lambda}{\Lambda^2 + \beta_1} \right) \mathbf{U}^T \tilde{\boldsymbol{\varepsilon}}. \quad (13)$$

Consider the case when  $\Lambda \gg (\beta_2, \beta_1)$ , then the terms inside the bracket cancel each other. For the case  $\Lambda \rightarrow 0$ , the term has insignificant contribution as well. We consider another case when the reference models are close enough such that regularization parameters differ by a small amount, i.e.  $\beta_2 = \beta_1 + \delta\beta$ . Substituting this in equation (13), the difference in the noise term is given by

$$\begin{aligned} & [\mathbf{H}^{-1}(\beta_2) - \mathbf{H}^{-1}(\beta_1)] \tilde{\mathbf{G}}^T \tilde{\boldsymbol{\varepsilon}} \\ &= \mathbf{V} \left( \frac{\Lambda}{\Lambda^2 + \beta_1} \left( 1 + \frac{\delta\beta}{\Lambda^2 + \beta_1} \right)^{-1} - \frac{\Lambda}{\Lambda^2 + \beta_1} \right) \mathbf{U}^T \tilde{\boldsymbol{\varepsilon}}. \end{aligned} \quad (14)$$

We expand the inverse power series and neglect terms of second and higher orders. Therefore to the first order, equation (14) is given by

$$\begin{aligned} & [\mathbf{H}^{-1}(\beta_2) - \mathbf{H}^{-1}(\beta_1)] \tilde{\mathbf{G}}^T \tilde{\boldsymbol{\varepsilon}} \\ &= \mathbf{V} \left( \frac{\Lambda}{\Lambda^2 + \beta_1} \left( 1 - \frac{\delta\beta}{\Lambda^2 + \beta_1} \right) - \frac{\Lambda}{\Lambda^2 + \beta_1} \right) \mathbf{U}^T \tilde{\boldsymbol{\varepsilon}} \\ &= -\mathbf{V} \left( \frac{\Lambda\delta\beta}{(\Lambda^2 + \beta_1)^2} \right) \mathbf{U}^T \tilde{\boldsymbol{\varepsilon}}. \end{aligned} \quad (15)$$

The quantity inside the bracket can be small when the denominator is much larger than the numerator. For  $\Lambda \rightarrow 0$  and  $\Lambda \gg \beta_1$  the diagonal matrix in equation (15) vanishes. For  $\Lambda \approx \beta_1$  the diagonal matrix reduces to  $\delta\beta/\beta_1^3$  which is also a small quantity if  $\delta\beta/\beta_1 < 1$ . Therefore we would expect that the contribution of this term to the overall region of data influence measure is small.

#### Analysis of the resolution matrix projected on to reference models ( $\mathbf{R}_2\mathbf{m}_0^2 - \mathbf{R}_1\mathbf{m}_0^1$ )

The SVD representation of this term from equation (12) is given by

$$(\mathbf{R}_2\mathbf{m}_0^2 - \mathbf{R}_1\mathbf{m}_0^1) = \mathbf{V} \left( \frac{\Lambda^2}{\Lambda^2 + \beta_2} \mathbf{V}^T \mathbf{m}_0^2 - \frac{\Lambda^2}{\Lambda^2 + \beta_1} \mathbf{V}^T \mathbf{m}_0^1 \right). \quad (16)$$

We apply the same argument that the reference models are close enough so that we can write  $\beta_2 = \beta_1 + \delta\beta$ , and we

obtain

$$\begin{aligned} (\mathbf{R}_2\mathbf{m}_0^2 - \mathbf{R}_1\mathbf{m}_0^1) &= \mathbf{V} \left( \frac{\Lambda^2}{\Lambda^2 + \beta_1} \right) \mathbf{V}^T (\mathbf{m}_0^2 - \mathbf{m}_0^1) \\ &\quad - \mathbf{V} \left( \frac{\Lambda^2\delta\beta}{(\Lambda^2 + \beta_1)^2} \right) \mathbf{V}^T \mathbf{m}_0^2. \end{aligned} \quad (17)$$

We can write the following equation to the first order by neglecting the second term in equation (17); we obtain

$$(\mathbf{R}_2\mathbf{m}_0^2 - \mathbf{R}_1\mathbf{m}_0^1) \approx \mathbf{V} \left( \frac{\Lambda^2}{\Lambda^2 + \beta_1} \right) \mathbf{V}^T (\mathbf{m}_0^2 - \mathbf{m}_0^1). \quad (18)$$

Equation (18) shows that to a first order, the term ( $\mathbf{R}_2\mathbf{m}_0^2 - \mathbf{R}_1\mathbf{m}_0^1$ ) is the projection of  $\mathbf{R}_1$  on to  $(\mathbf{m}_0^2 - \mathbf{m}_0^1)$ .

#### Analysis of the resolution matrix projected on to the true model ( $\mathbf{R}_2 - \mathbf{R}_1$ ) $\mathbf{m}$

The SVD expansion of this term from equation (12) is given by

$$(\mathbf{R}_2 - \mathbf{R}_1) \mathbf{m} = \mathbf{V} \left( \frac{\Lambda^2}{\Lambda^2 + \beta_2} - \frac{\Lambda^2}{\Lambda^2 + \beta_1} \right) \mathbf{V}^T \mathbf{m}. \quad (19)$$

Writing  $\beta_2 = \beta_1 + \delta\beta$  and applying the first-order approximation, we obtain

$$(\mathbf{R}_2 - \mathbf{R}_1) \mathbf{m} = -\mathbf{V} \left( \frac{\Lambda^2\delta\beta}{(\Lambda^2 + \beta_1)^2} \right) \mathbf{V}^T \mathbf{m}. \quad (20)$$

Using a similar argument to that used in equation (17), the contribution of the term  $(\mathbf{R}_2 - \mathbf{R}_1) \mathbf{m}$  to the region of data influence measure is also negligible. Thus, if we combine the results of equations (15), (17) and (20), we obtain

$$\begin{aligned} \hat{\mathbf{m}}_2 - \hat{\mathbf{m}}_1 &= (\mathbf{I} - \mathbf{R}_1) (\mathbf{m}_0^2 - \mathbf{m}_0^1) - \mathbf{V} \left( \frac{\Lambda^2\delta\beta}{(\Lambda^2 + \beta_1)^2} \right) \\ &\quad \times \mathbf{V}^T (\mathbf{m} - \mathbf{m}_0^2) - \mathbf{V} \left( \frac{\Lambda\delta\beta}{(\Lambda^2 + \beta_1)^2} \right) \mathbf{U}^T \tilde{\boldsymbol{\varepsilon}}. \end{aligned} \quad (21)$$

Equation (21) is the expression connecting the region of data influence and the resolution matrices when the regularization perturbation between the two inversions is of first order, i.e. the change in the regularization parameter between the two inversions using the two reference models is not too large, such that  $O(\|\delta\beta\|^2) \rightarrow 0$ . Neglecting the contribution of the second and the third terms in equation (21) and denoting  $\mathbf{R} = \mathbf{R}_1$ , we obtain

$$\begin{aligned} \hat{\mathbf{m}}_2 - \hat{\mathbf{m}}_1 &\approx (\mathbf{m}_0^2 - \mathbf{m}_0^1) - \mathbf{V} \left( \frac{\Lambda^2}{\Lambda^2 + \beta_1} \right) \mathbf{V}^T (\mathbf{m}_0^2 - \mathbf{m}_0^1) \\ &= (\mathbf{I} - \mathbf{R}) (\mathbf{m}_0^2 - \mathbf{m}_0^1). \end{aligned} \quad (22)$$

This approximate relationship shows that the difference between the two inversions in the estimated models is the projection of the blurring operator  $(\mathbf{I} - \mathbf{R})$  on to the differenced reference models. For a linear problem, it formally establishes the connection between the region of data influence (RDI) measure and the resolution matrix. In terms of each element, equation (22) can be written as

$$(\hat{\mathbf{m}}_2 - \hat{\mathbf{m}}_1)_k \approx (\mathbf{m}_0^2 - \mathbf{m}_0^1)_k - (\mathbf{r}^k)^T (\mathbf{m}_0^2 - \mathbf{m}_0^1). \quad (23)$$

If the rows of the resolution matrix  $\mathbf{r}^k = (0, \dots, 0, 0, \dots, 0)$ , then  $RDI = 1$ , indicating poor resolution. In the regions where  $\mathbf{r}^k = \delta_k = (0, \dots, 0, 1, 0, \dots, 0)$ , the difference in equation (23) approaches zero, thus  $RDI = 0$ , indicating good resolution. A further simplification can be made if we assume that the two reference models are constant and equal to two different homogeneous half-space values. This is commonly used in the region of data influence (RDI) approach (Oldenburg and Li 1999). Writing  $(\mathbf{m}_0^2 - \mathbf{m}_0^1) = \alpha \mathbf{e}$  where  $\mathbf{e}$  is a vector of ones and  $\alpha$  is a constant equal to the difference of the half-space values, then  $RDI$  for the  $k$ th cell is given by  $(\hat{\mathbf{m}}_2 - \hat{\mathbf{m}}_1)_k / \alpha \approx \sum (\mathbf{I} - \mathbf{R})_k$ , i.e. it is equal to the summation of the  $k$ th row of the blurring function  $(\mathbf{I} - \mathbf{R})$ . Thus the  $RDI$  of the  $k$ th cell can be written as

$$RDI_k \approx \sum_j (1 - r_{kj}), \quad (24)$$

where  $r_{kj}$  is the  $j$ th element in the  $k$ th row of the resolution matrix.

We note that the region of data influence measure given in equation (7) is the ratio of the difference between the two inverted models to the difference between the two reference models. In the limit that the two reference models are close enough, the region of data influence measure can be mathematically stated as the derivative of the inverted model with respect to the change in the reference model. Therefore to derive the relationship between the region of data influence and the resolution matrix, we assumed that the two reference models are close enough so that the difference in regularization is not significant. Equation (22) was obtained using SVD analysis by considering the model weighting as diagonal. For a general model weighting matrix, a similar expression can be derived as shown in Appendix B.

An important point to note is that the region of data influence measure is dependent on the averaging kernels, i.e. rows of the resolution matrix and not the point spread functions. So the spread from the point spread functions can potentially provide a different resolution measure. In the next section, using a linear example, we provide insight into the relationship between the region of data influence and resolution matrix and we demonstrate the similarities and differences between these two measures.

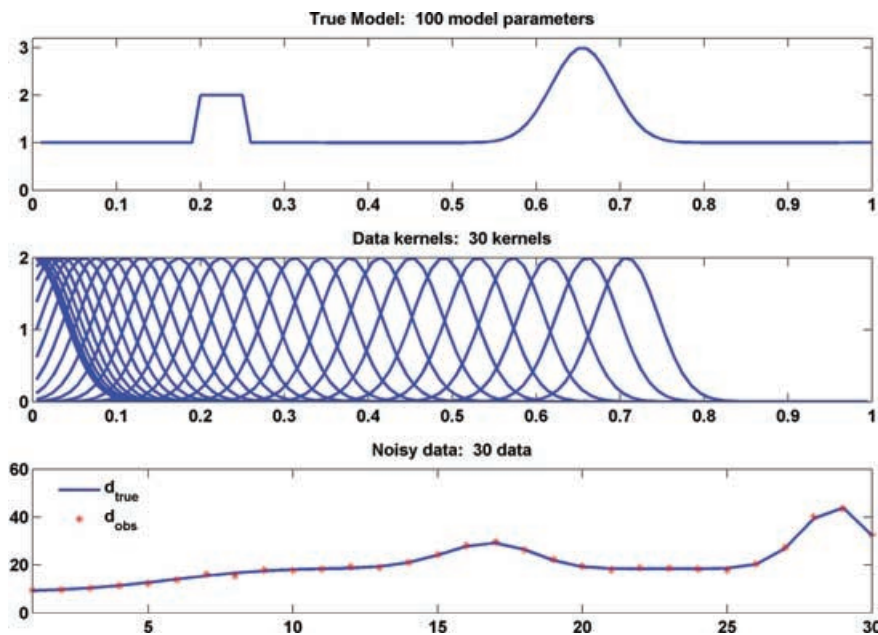


**Figure 1** Plots of the model, kernels and data for the linear example. The top plot shows the true model. The horizontal axis is distance and the vertical axis is amplitude. The centre plot shows the Gaussian data kernels used for the example. The bottom plot shows the true data and the observed data, contaminated with 2% standard deviation random noise.

## LINEAR EXAMPLE

We consider a 1D, linear inverse problem of the form  $\mathbf{d}_j = (g_j, \mathbf{m})$ , where the data kernels are blurry Gaussian functions commonly used in computer scale vision problems, given by  $g_j = A \exp\left(-\frac{(x-x_j)^2}{4\sigma^2}\right)$ , where  $A = 2.0$  and  $\sigma = 0.026$  for our particular example. Using a synthetic model vector with 100 parameters, we generated 30 data observations and contaminated these data with Gaussian random noise.

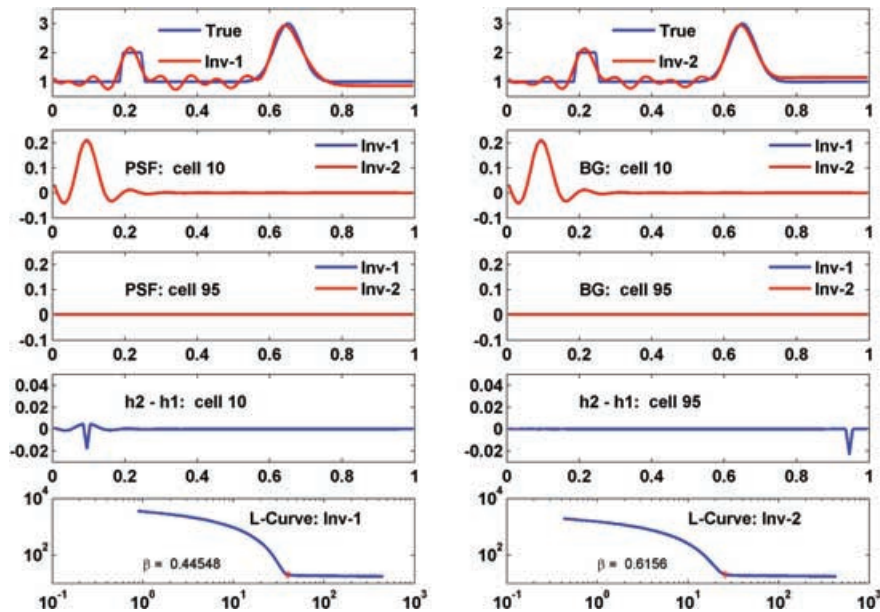
Figure 1 shows the true model, the Gaussian data kernels and the observed data. Next, we inverted the same data with two different objective functions, one designed to recover the smallest model and the other designed to recover a combination of the smallest and flattest models. This was accomplished by beginning with a general model objective function which is a combination of the smallness and flatness components, given by  $\phi_m = \alpha_s \|\mathbf{W}_s(\mathbf{m} - \mathbf{m}_0)\|^2 + \alpha_x \|\mathbf{W}_x(\mathbf{m} - \mathbf{m}_0)\|^2$  where  $\mathbf{W}_s$  is a smallest model weighting matrix that is effectively a diagonal matrix, and  $\mathbf{W}_x$  is the flattest model weighting matrix which is the discrete form of the first-derivative operator to impose smoothness in the solution.  $\alpha_s$  and  $\alpha_x$  are the control parameters chosen to weigh the relative contribution of smallness versus flatness. An L-curve criterion (Hansen 1992) was used to select the value of the regularization parameter for each inversion.

## Inversion with only the smallest component

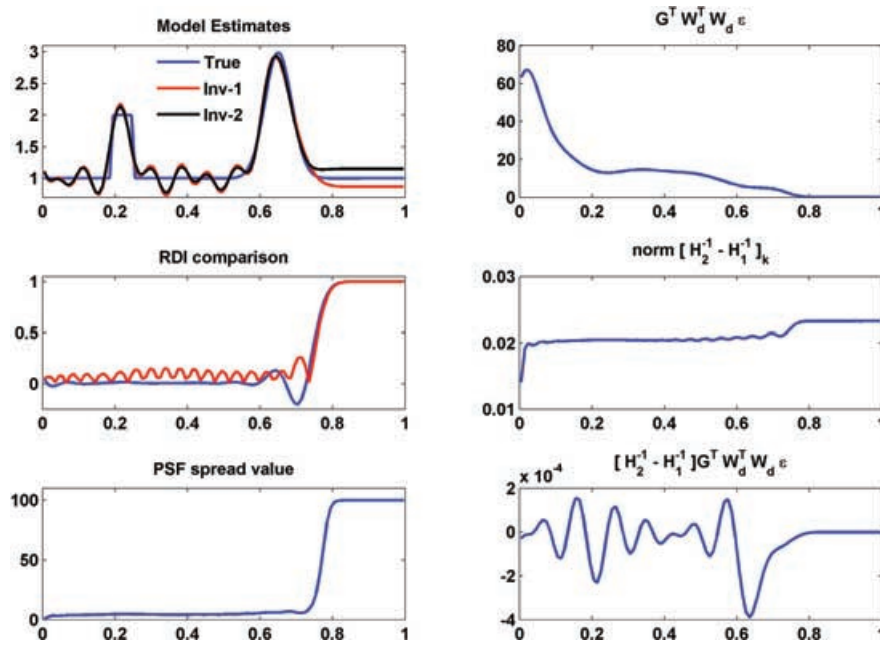
First, we consider only a smallest model component by choosing  $\alpha_s = 1$ ,  $\alpha_x = 0$ . The choice of smallest model weighting produces a diagonal matrix and the inversion has the ability to recover the reference model when data kernels are non-informative.

Figure 2 shows a comparison of the two inverted models using the different reference models ( $\mathbf{m}_{\text{ref}}^1 = 0.8696$ ,  $\mathbf{m}_{\text{ref}}^2 = 1.15$ ) and plots of point spread functions and Bachus–Gilbert kernels from different portions of the model. From Fig. 2, we see that the resolution in the 10th cell is significantly better than that in the 95th cell. The flat point spread function and averaging kernel for the 95th cell clearly demonstrate the lack of resolution. The third panels in Fig. 2 show the difference in the inverse Hessian matrix for the 10th ( $x = 0.1$ ) and 95th ( $x = 0.95$ ) cells. In each case, this difference is small because of the small difference in the regularization parameter. The bottom plots in Fig. 2 show the L-curves used in selecting the regularization parameters for the two separate inversions.

The top left-hand plot in Fig. 3 shows the two inverted models as well as the true model. Note that both estimated models clearly revert back to their respective reference models beyond depth of  $x = 0.75$ . The middle left-hand plot in Fig. 3 shows the region of data influence measure computed using two



**Figure 2** For this set of plots, we consider a model objective function containing only a smallness component ( $\alpha_s = 1.0$ ;  $\alpha_x = 0$ ), thus the model weighting matrix is the identity matrix. The top panel shows the comparison between the true and recovered models for constant reference model values of 0.8696 (Inv-1) and 1.15 (Inv-2). The second panel shows the point spread functions (PSFs) and Bachus–Gilbert kernels for Inv-1 and Inv-2 at the 10th cell ( $x = 0.10$ ). The third panel shows a similar comparison at the 95th cell ( $x = 0.95$ ). The fourth panel shows the difference in the inverse Hessian matrix for inversion 1 and inversion 2 at the 10th and 95th cells. The bottom panel shows the L-curve ( $\phi_d$  vs.  $\phi_m$ ) used to select the regularization parameter.



**Figure 3** For this set of plots,  $\alpha_s = 1.0$  and  $\alpha_x = 0$ , as in Fig. 2. The top left-hand plot shows a comparison between the recovered models and the true model. The middle left-hand plot shows a comparison of the region of data influence (RDI) computed using equation (7) (red) and the region of data influence computed using the approximation in equation (24) (blue). The bottom left-hand plot shows the point spread function (PSF) spread. The three plots on the right show a graphical view of the terms in equation (10). The top right-hand plot shows the  $\mathbf{G}^T \mathbf{W}_d^T \mathbf{W}_d \boldsymbol{\varepsilon}$  term. The middle right-hand plot shows the norm of the difference in the rows of the inverse Hessian matrices. The bottom right-hand plot shows that the contribution of the term  $[\mathbf{H}_2^{-1} - \mathbf{H}_1^{-1}] \mathbf{G}^T \mathbf{W}_d^T \mathbf{W}_d \boldsymbol{\varepsilon}$  to the region of data influence is minimal.

separate methods, one using the exact method of equation (7) and the other using the approximation from equation (24). Note that although there are differences between the two region of data influences, both indicate good resolution up to a depth of  $x = 0.75$  and a loss in resolution beyond this distance. The same can be said for the point spread function spread value shown in the bottom left-hand plot of Fig. 3. The three right-hand panels in Fig. 3 provide a graphical view of some of the terms from equation (10). The top right-hand panel in Fig. 3 shows the  $\mathbf{G}^T \mathbf{W}_d^T \mathbf{W}_d \boldsymbol{\varepsilon}$  term. Note that where resolution is good, this quantity is non-zero, but where resolution is poor, this quantity goes to zero. The middle right-hand plot in Fig. 3 shows the norm of the difference in the rows of the inverse Hessian matrices. Note that the difference is small everywhere because of the diagonal model weighting and the small difference in the regularization parameters. The bottom right-hand plot in Fig. 3 shows that when these two quantities are multiplied, the result is small everywhere, i.e.  $[\mathbf{H}_2^{-1} - \mathbf{H}_1^{-1}] \mathbf{G}^T \mathbf{W}_d^T \mathbf{W}_d \boldsymbol{\varepsilon} \approx 0$ , and makes a minimal contribution to the difference in the model estimates in equation (10).

#### Inversion with flattest and smallest component

Next we consider a more general case where the model objective function contains both a smallness component and a

flatness component so that the model-weighting matrix is no longer a diagonal matrix. We chose  $\alpha_s = 10$ ,  $\alpha_x = 1$  for our computations.

Figure 4 first shows a comparison of the two inverted models using the different reference models ( $\mathbf{m}_{\text{ref}}^1 = 0.10$ ,  $\mathbf{m}_{\text{ref}}^2 = 10$ ) and plots of point spread functions and Bachus–Gilbert kernels from different portions of the model. From Fig. 4, we see that the resolution in the 10th cell is again significantly better than the 95th cell. The flat point spread function for the 95th cell clearly demonstrates a lack of resolution. However, the averaging kernel for the 95th cell shows a peak, indicating that the average value is non-zero, although this peak is shifted well to the left of the region of interest. This clearly demonstrates the difference between point spread functions and Bachus–Gilbert kernels. In the regions where there is no resolution, there is no purpose in considering the credibility of the average value and hence these regions should be removed from any further interpretation. The bottom plots in Fig. 4 show the L-curves used in selecting the regularization parameters.

The top left-hand plot in Fig. 5 shows the two inverted models as well as the true model. Note that both estimated models attempt to revert back to their respective reference models beyond approximately  $x = 0.75$ . However, in the



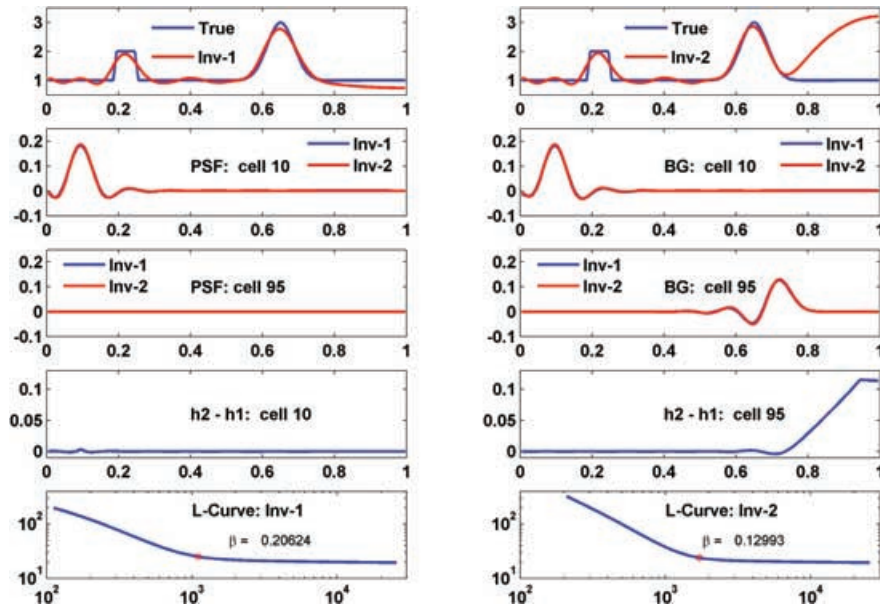


**Figure 4** For this set of plots, we consider a model objective function containing both a flatness ( $\alpha_x = 1$ ) and a smallness ( $\alpha_s = 10$ ) component, thus the model weighting matrix is not the identity matrix. The top panel shows the comparison between the true and recovered models for constant reference model values of 0.10 (Inv-1) and 10 (Inv-2). The second panel shows the point spread functions (PSFs) and Bachus–Gilbert kernels for Inv-1 and Inv-2 at the 10th cell ( $x = 0.10$ ). The third panel shows a similar comparison at the 95th cell ( $x = 0.95$ ). The fourth panel shows the difference in the inverse Hessian matrix for inversion 1 and inversion 2 at the 10th and 95th cells. The bottom panel shows the L-curve ( $\phi_d$  vs.  $\phi_m$ ) used to select the regularization parameter.

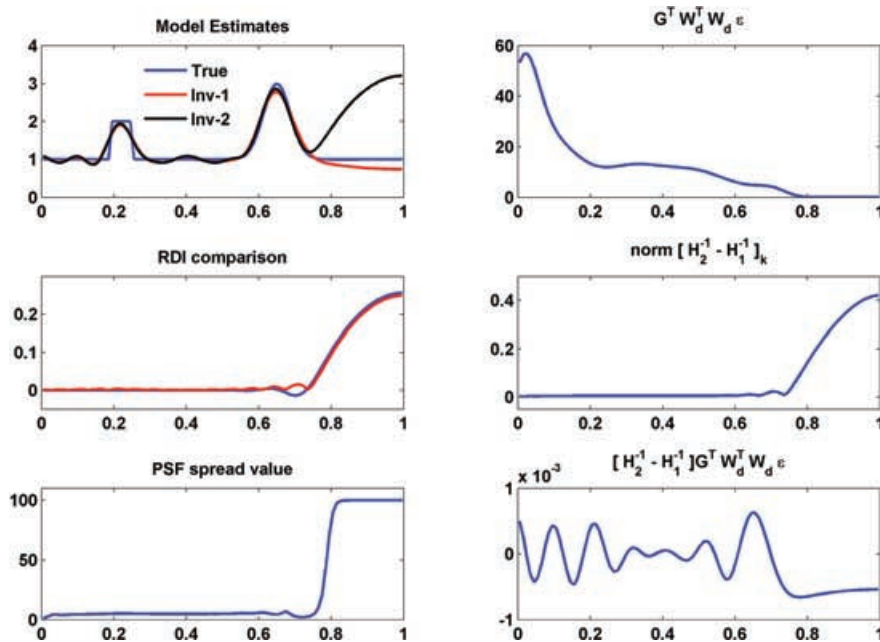


**Figure 5** For this set of plots,  $\alpha_x = 1$  and  $\alpha_s = 10$ , as in Fig. 4. The top left-hand plot shows a comparison between the recovered models and the true model. The middle left-hand plot shows a comparison of the region of data influence (RDI) computed using equation (7) (red) and the region of data influence computed using the approximation in equation (24) (blue). The bottom left plot shows the point spread function (PSF) spread. The three plots on the right show a graphical view of the terms in equation (10). The top right-hand plot shows the  $G^T W_d^T W_d \epsilon$  term. The middle right-hand plot shows the norm of the difference in the rows of the inverse Hessian matrices. The bottom right-hand plot shows that the contribution of the term  $[H_2^{-1} - H_1^{-1}] G^T W_d^T W_d \epsilon$  to the region of data influence is minimal.

case of inversion 2 where the reference model equals 10, the smoothing imposed by the model objective function does not allow for the inverted model to revert completely back to the reference model. The middle left-hand plot in Fig. 5 shows the region of data influence measure computed using two separate methods, one using the exact method of equation (7) and the other using the approximation from equation (24). There are minor differences between the two region of data influences, but both indicate good resolution up to approximately  $x = 0.75$  and a loss in resolution beyond this distance. The region of data influence does not reach a value of unity because the imposed model smoothing does not allow the inverted result to revert fully back to the reference model in the region where the resolution is poor. The bottom left-hand plot of Fig. 5 shows the point spread function spread value. The point spread function spread looks similar to the spread computed in the smallest model case suggesting that the region of data influence and the point spread function spread are two different resolution measures. Note that both the region of data influences ratio and the spread indicate a loss in resolution beyond  $x \sim 0.75$ , corresponding to the distance at which the recovered models for the two inversions diverge to their respective reference models, i.e. beyond this location, the recovered models are insensitive to the available data.

The three plots on the right side of Fig. 5 provide a graphical view of some of the terms from equation (10). The top right-hand plot in Fig. 5 shows the  $\mathbf{G}^T \mathbf{W}_d^T \mathbf{W}_d \boldsymbol{\varepsilon}$  term. Note that, similarly to the smallest model case, where resolution is good, this quantity is non-zero, but where resolution is poor, this quantity goes to zero. The middle right-hand plot in Fig. 5 shows the norm of the difference in the rows of the inverse Hessian matrices. Note that the difference is small when resolution is good and large when resolution is poor, which is the exact opposite of the  $\mathbf{G}^T \mathbf{W}_d^T \mathbf{W}_d \boldsymbol{\varepsilon}$  term shown in the top right-hand plot. The bottom right-hand plot in Fig. 5 shows that when these two quantities are multiplied the result is small everywhere, i.e.  $[\mathbf{H}_2^{-1} - \mathbf{H}_1^{-1}] \mathbf{G}^T \mathbf{W}_d^T \mathbf{W}_d \boldsymbol{\varepsilon} \approx 0$ , and makes a minimal contribution to the difference in the model estimates in equation (10) and thus, by extension, makes a minimal contribution to the region of data influence measure.

## NON-LINEAR EXAMPLES

We further demonstrate the use of the point spread function spread and the region of data influence ratio with examples from controlled-source electromagnetics. The particular physical experiment considered here is controlled-source audio-frequency magnetotellurics (CSAMT). CSAMT is a frequency-

domain electromagnetic sounding experiment which has been applied to a number of problems, such as minerals exploration, geothermal exploration, groundwater investigations and structural analysis (Zonge and Hughes 1991). For both examples, the CSAMT source considered is an earthed electric dipole of finite length with a frequency range of 0.5 to 8192 Hz.

### Synthetic CSAMT example

Using a five-layer, 1D earth conductivity model, containing a shallow resistive region and a deeper conductive region, we computed the electric and magnetic field data at a single receiver location. The transmitter for this example is 1 km in length and is orientated in the east–west direction. The receiver location is 2 km north of and centred on the transmitter. Note that this receiver location will be in the strong signal zone for the  $E_x$ ,  $H_y$ , and  $H_z$  components and in the null zone for the  $E_y$  and  $H_x$  components. For this reason, the results shown for this example primarily consider the  $E_x$ ,  $H_y$  and  $H_z$  components.

The frequency range for the synthetic experiment was from 0.5 Hz to 8192 Hz. Data were computed for five field components ( $E_x$ ,  $E_y$ ,  $H_x$ ,  $H_y$ ,  $H_z$ ). These data were then contaminated with noise, with a standard deviation based on 5% of the observed amplitudes and  $2^\circ$  for phases (Fig. 6). We inverted these data for an 80-layer earth conductivity model using a non-linear Gauss–Newton approach (Routh and Oldenburg 1999).

Figures 7 and 8 show some point spread functions and averaging kernels selected from the conductive and resistive regions of the model. Although the inverted model estimates (Figs 7 and 8) vary, depending on the field data combination chosen for inversion, it is clear that resolution is better in the conductive region compared to the resistive region, which is expected in electromagnetic imaging experiments. Also note that the resolution and the model recovery is better in those inversions that include the  $E_x$ -component.

The linearized resolution matrices for the various field data combinations are shown in Fig. 9. Note that the resolution drops off for all inversions in the vicinity of 1 km depth. It is clear that resolution is significantly degraded at depth; however, the inversions using the electric field component show a slightly greater resolved depth interval. This increased depth of investigation becomes more obvious when we compute the spread value for each of the inversions.

Figure 10 show that the inversions containing only magnetic field data have a diminished depth of investigation when compared to the inversions containing the electric field component.

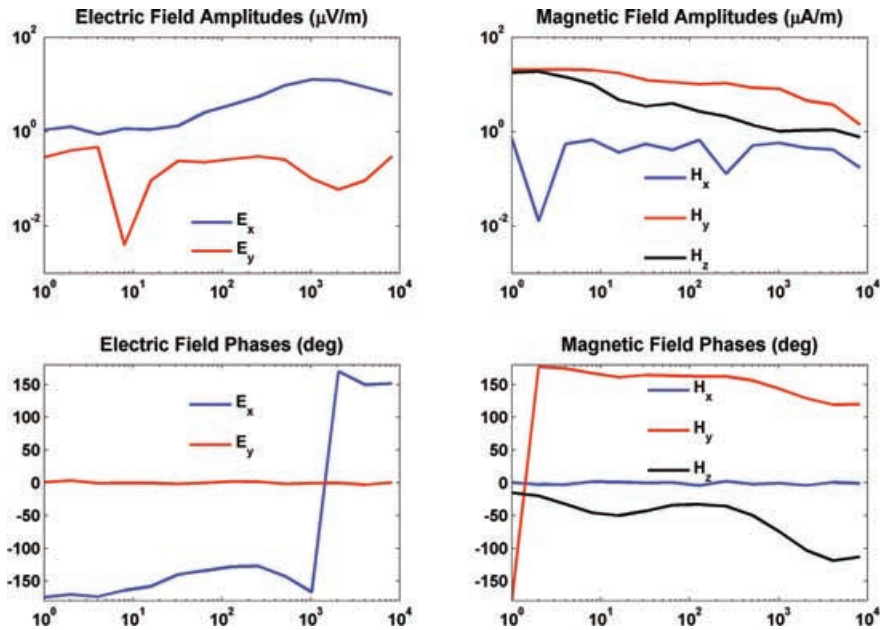


**Figure 6** Electric and magnetic field data versus frequency with random noise added. The standard deviation is based on 5% of observed amplitudes and  $2^\circ$  for phases. The horizontal axis for all plots is frequency (Hz). The vertical axis for the top left-hand plot is electric field amplitude ( $\mu\text{V/m}$ ); the vertical axis for the top right-hand plot is magnetic field amplitude ( $\mu\text{A/m}$ ); the vertical axis for the bottom two plots is phase ( $^\circ$ ).

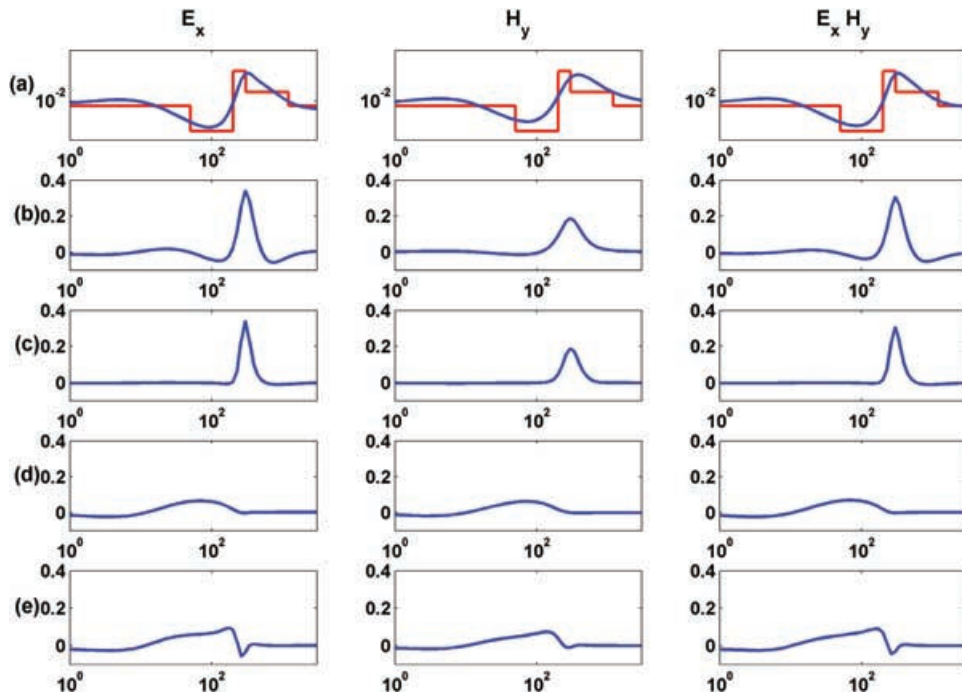


**Figure 7** Model estimates and selected point spread functions and averaging kernels for the inversion of  $E_x$  (left-hand column),  $H_y$  (centre column), and  $E_x H_y$  (right-hand column). The horizontal axis for all plots is depth (m). Row (a) shows the model estimate (blue) and the true model (red) for the three separate inversions. The vertical axis is electrical conductivity (S/m). For remaining plots (rows b,c,d,e), the vertical axis is dimensionless amplitude of  $R$ . Rows (b) and (c) show the point spread functions and the averaging kernels for the conductive region, respectively. Rows (d) and (e) are the point spread functions and the averaging kernels for the resistive region, respectively.

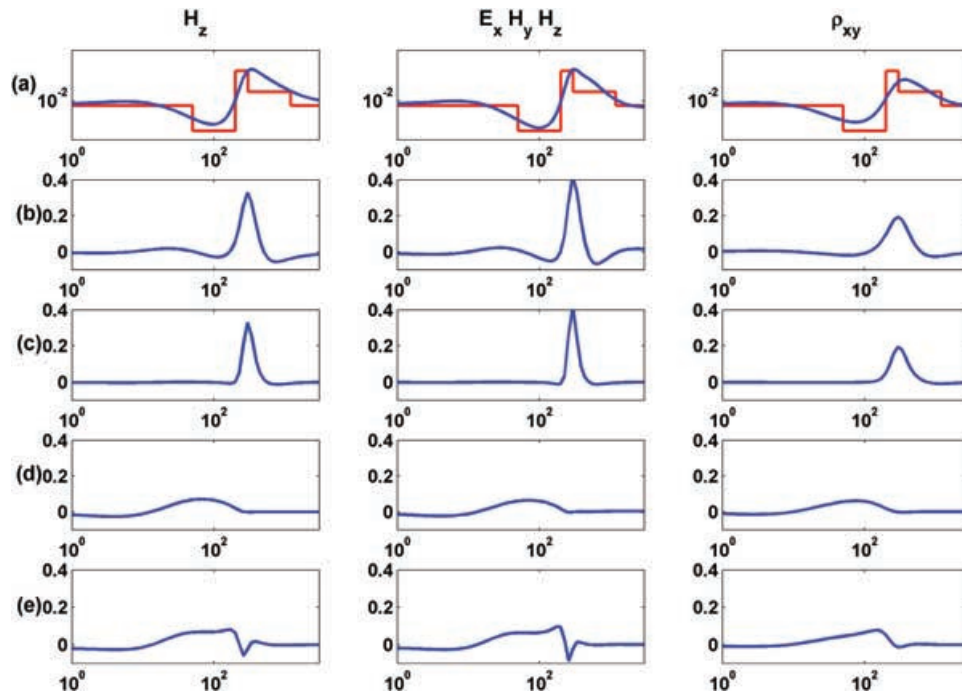


**Figure 8** Model estimates and selected point spread functions and averaging kernels for the inversion of  $H_z$  (left-hand column),  $E_x H_y H_z$  (centre column), and  $D_{xy}$  (right-hand column). The horizontal axis for all plots is depth (m). Row (a) shows the model estimate (blue) and the true model (red) for the three separate inversions. The vertical axis is electrical conductivity (S/m). For remaining plots (rows b,c,d,e), the vertical axis is dimensionless amplitude of the resolution matrix. Rows (b) and (c) show the point spread functions and the averaging kernels for the conductive region, respectively. Rows (d) and (e) are the point spread functions and the averaging kernels for the resistive region, respectively.

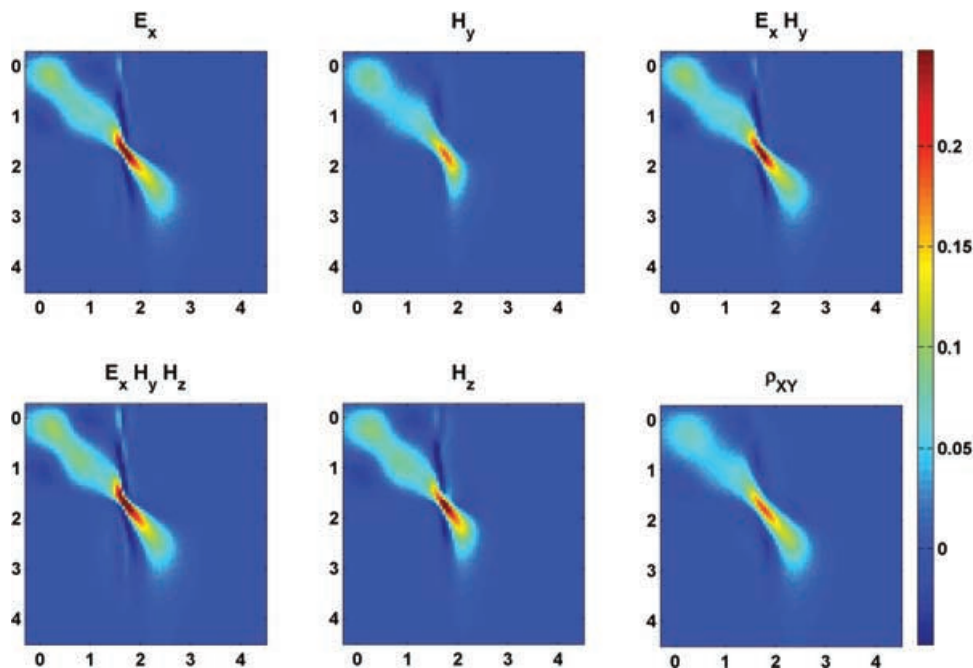


**Figure 9** Linearized resolution matrices from inversion of various field component combinations. Horizontal and vertical axes are  $\log_{10}$ (depth) in metres. The colour bar on the right is common to all of the figures, and corresponds to the dimensionless amplitude of the resolution matrix.

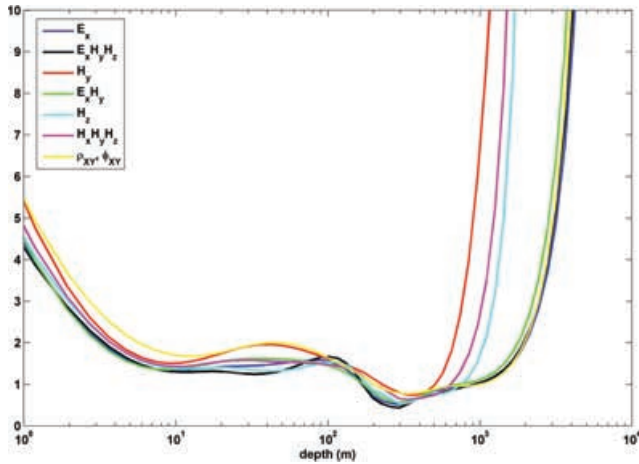


**Figure 10** Point spread function spread value at the final iteration of the inversions. The horizontal axis is depth (m). This plot clearly shows a distinction in the depth of investigation for those inversions including the  $E_x$ -component and those using only the magnetic field data.

If we choose an iso-spread value (here we have chosen a value of 3), we can then compute the depth of investigation for the various inversions (Fig. 11). In fact, when we do this, we see that there is diminished resolution both in the near surface and at depth so that we are able to define an interval over

which we may then interpret the results of our inverted models (Fig. 12).

Figure 13 shows the region of data influence for the various data combinations. In this case, the region of data influence curves provide very similar information to that provided by the spread curves in Fig. 10. We see that the inversions including the  $E_x$ -component have a depth of investigation that is better than those inversions considering only the magnetic field components and that resolution is poor for all the inversions within the padding region of the inverted model. We recognize that the choice of an iso-spread in the case of point spread function spread and the choice of an index value in the case of region of data influence are subjective, and these choices will ultimately affect which regions of the model will be interpreted. Once the choice is made it provides the demarcation between the good and bad regions of the model resolved by the data. In spite of this subjectivity, the flexibility of having these measures provides a useful interpretation capability that is of practical value.

#### Field CSAMT example

In this section we present the analysis of the point spread function spread and the region of data influence measure for a real data set. CSAMT data were collected in order to

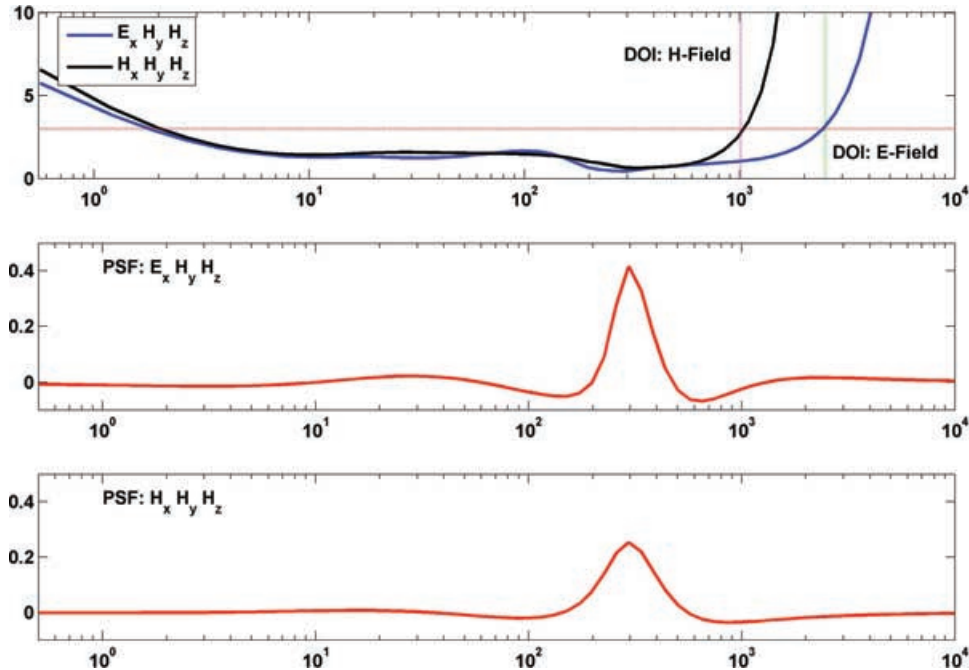


**Figure 11** The top panel shows the spread curves for the  $E_x H_y H_z$  (blue) and  $H_x H_y H_z$  (black) field inversions. The horizontal line indicates an iso-spread value of 3 chosen to examine the depth of investigation of the fields. Point spread functions within the conductive layer are shown in the middle ( $E_x H_y H_z$ ) and bottom ( $H_x H_y H_z$ ) panels. The horizontal axis for all three plots is depth (m), and the vertical axis is dimensionless amplitude.



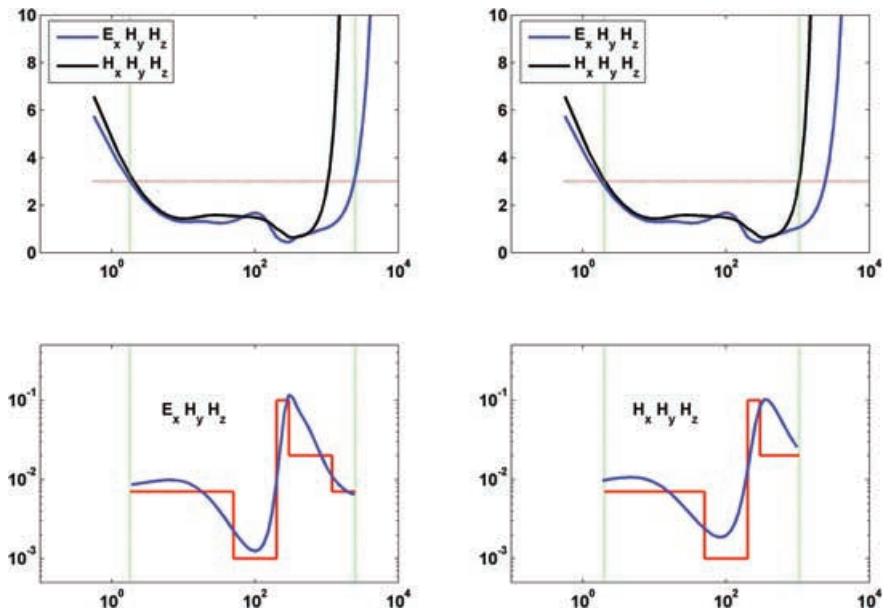


**Figure 12** The top panels show the point spread function spread curves for the  $E_x H_y H_z$  (blue) and  $H_x H_y H_z$  (black) field inversions. The horizontal dashed lines show the chosen iso-spread value of 3. The vertical dashed lines show the depth intervals resolved by the data, based on this choice of iso-spread value. The bottom panels show the truncated models. The horizontal axis for all four plots is depth (m), the vertical axis for the upper plots is dimensionless amplitude, and for the lower plots it is electrical conductivity (S/m).

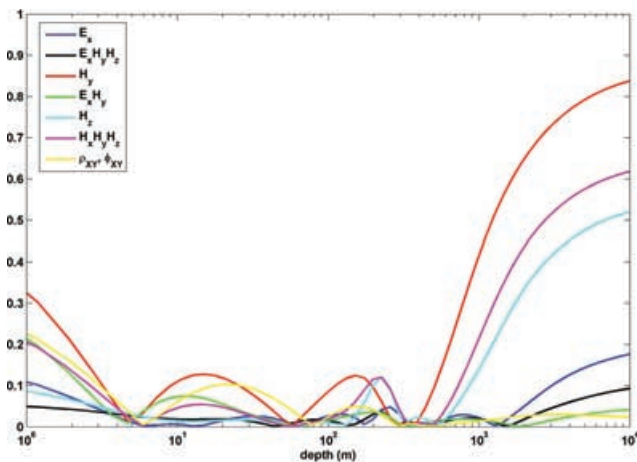


**Figure 13** Region of data influence curves for various field component inversions. The horizontal axis is depth (m). The region of data influence plot, like the spread plot (see Fig. 10), clearly shows a distinction between the depths of investigation for those inversions including the electric field data and those only using the magnetic field data.

characterize a geothermal prospect in south-western Idaho, USA. The source was a 1400 m long earthed electric dipole, located approximately 6 km from the receiver line (Fig. 14). Here, we present results of inversion of the amplitude of the  $x$ -component of the electric field for 56 receiver stations. These data were measured at 25 frequencies ranging from 1 to

8192 Hz. The reference model used was a 100  $\Omega\text{m}$  half-space. To calculate the region of data influence ratio, we also inverted these data with reference models of 10  $\Omega\text{m}$  and 1000  $\Omega\text{m}$ . In each case, we inverted for a 1D, 60-layer earth model with layer thickness increasing logarithmically with depth, using a noise assumption of 5% of the observed electric field amplitudes.

Figure 15 shows the generally good agreement between the observed and predicted data. The majority of these data were fit within a  $\chi^2$  misfit criterion of one. Results for those data that were not fitted within this criterion were discarded from further analysis. Figure 16 shows the inverted model to a depth of 1200 m, and the spread and region of data influence plots for the entire model depth. Note that for the region of the model that we are interested in, i.e. from approximately 100 to 500 metres depth, the resolution is good according to both the region of data influence and the spread plot, so we are able to interpret this portion of the model with improved confidence, compared to the very shallow or very deep regions of the model. Both the spread plot and the region of data influence plot show a well-resolved interval between 10 and 1000 metres. This is the depth interval hypothesized to contain the primary flow conduits for the geothermal system, thus the more conductive regions within the conductivity image are likely to correspond to the location of geothermal fluids.

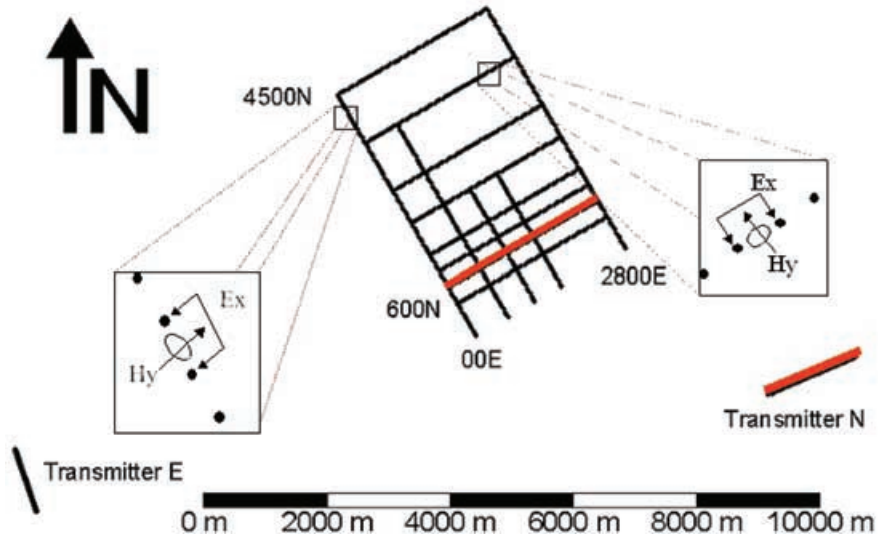


Figure 14 Map view of CSAMT survey in south-west Idaho, USA. We show results from transmitter N, and receiver line 900N, indicated by the thick red lines on the map.

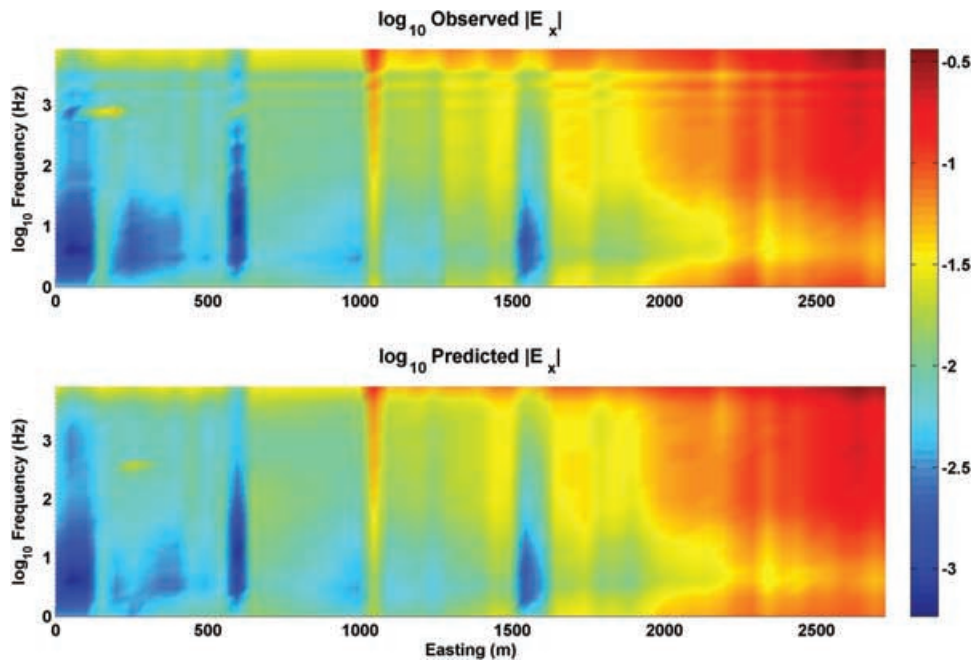


Figure 15 Observed (top plot) and predicted (bottom plot) electric field amplitude data for Line 900N. The colour bar on the right is common to both plots, and corresponds to  $\log_{10}(|E_x|)$  ( $\mu\text{V/m}$ ).

Unfortunately we do not have any borehole information to verify the result but the presence of hot fluids in surface springs indicates the presence of geothermal fluids in the subsurface.

## CONCLUSIONS

It is important to demonstrate the credibility of the subsurface images obtained from geophysical data, particularly when in-

ferences and decisions are made, based on the images. Therefore, in addition to computing the final images, further analysis should be carried out using various appraisal tools to evaluate which parts of the model are more believable than others. Even at a very simplistic level, this knowledge is useful for aiding model interpretation. Depending on which specific questions need to be answered based on the geophysical images, the appraisal analysis can be appropriately formulated. We have

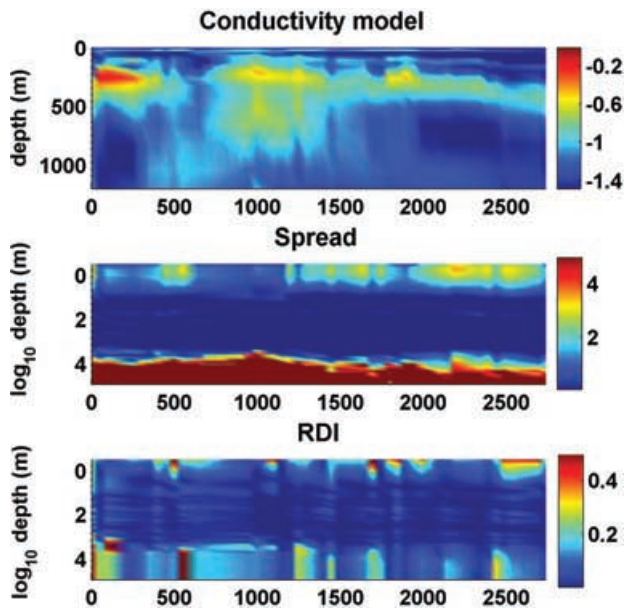


Figure 16 Model and resolution for Line 900N. The top panel is the conductivity image to 1200 m depth with a colour bar that corresponds to  $\log_{10}(\sigma)$  (S/m). The middle panel is the point spread function spread value for the entire depth interval with the colour bar corresponding to the dimensionless spread amplitude. The bottom panel is the region of data influence (RDI) index for the entire depth interval with the colour bar corresponding to dimensionless region of data influence amplitude. The horizontal axis for all three plots is the distance (m) along the receiver line.

examined and compared the region of data influence measure, introduced by Oldenburg and Li (1999), and the spread, computed using linearized resolution analysis with point spread functions. If different appraisal tools provide similar answers then confidence in the model interpretation is enhanced.

In both region of data influence and point spread function spread measure, the threshold between good and bad resolution must be chosen. Although this is sometimes subjective, the value added by generating these measures far outweighs the subjectivity of choosing the threshold value. To gain insight into these two measures, we demonstrated the connection between them, i.e. the point spread function spread and the region of data influence, using a linear inverse problem. Although the connection is better understood for linear problems, we demonstrated via a numerical example that similar conclusions hold for a non-linear CSAMT inversion problem. An important difference is that the region of data influence seems to depend more strongly upon the averaging kernels (rows of resolution matrix) than on the point spread function (columns of resolution matrix). Synthetic examples demonstrate that the point spread function spread has more detailed

information about the resolution problem than the region of data influence. Although there are some differences in both approaches, overall they indicate similar information about better resolved regions both for synthetic and field examples. Using different appraisal tools for a problem can help us gain additional insight into the results of our inversions. This can lead to increased confidence in our solutions and help us to make better informed decisions.

## ACKNOWLEDGEMENTS

We thank Zonge Engineering and Prof. Paul Donaldson for permission to show the CSAMT data. C.M. is funded by a graduate fellowship from the Inland Northwest Research Alliance (INRA). We thank Prof. Doug Oldenburg for an excellent review and particularly for his suggestion to look into the smallest model example that provided insight into the problem and resulted in an improved manuscript. We also thank an anonymous reviewer who helped to bring more clarity to the paper. This research was funded by NSF EPSCOR award # EPS0132626 and EPA award #EPA-X-96004601.

## REFERENCES

- Alumbaugh D. and Newman G. 2000. Image appraisal in 2D and 3D electromagnetic inversion. *Geophysics* **65**, 1455–1467.
- Backus G. and Gilbert F. 1968. The resolving power of gross earth data. *Geophysical Journal of the Royal Astronomical Society* **16**, 169–205.
- Backus G. and Gilbert F. 1970. Uniqueness in the inversion of gross earth data. *Philosophical Transactions of the Royal Society, Series A, Mathematical and Physical Sciences* **266**, 123–192.
- Barnes A. 1993. Instantaneous spectral bandwidth and dominant frequency with seismic reflection data. *Geophysics* **58**, 419–428.
- Friedel S. 2003. Resolution, stability and efficiency of resistivity tomography estimated from a generalized inverse approach. *Geophysical Journal International* **153**, 306–316.
- Hansen P.C. 1992. Analysis of discrete ill-posed problems by means of L-curve. *SIAM Reviews* **34**, 561–580.
- Oldenborger G.A. 2006. *Advances in electrical resistivity tomography: modeling, electrode position errors, time-lapse monitoring of an injection/withdrawal experiment, and solution appraisal*. PhD thesis, Boise State University.
- Oldenburg D. 1983. Funnel functions in linear and nonlinear appraisal. *Journal of Geophysical Research* **B9**, 7387–7398.
- Oldenburg D. and Li Y. 1999. Estimating the depth of investigation in dc resistivity and IP surveys. *Geophysics* **64**, 403–416.
- Parker R. 1994. *Geophysical Inverse Theory*. Princeton University Press.
- Routh P. and Miller C. 2006. Image interpretation using appraisal analysis. *SAGEEP Proceedings*, 1812–1820.



- Routh P. and Oldenburg D. 1999. Inversion of controlled source audio-frequency magnetotelluric data for a horizontally layered Earth. *Geophysics* **64**, 1689–1697.
- Shearer P.M. 1999. *Introduction to Seismology*. Cambridge University Press.
- Sinha S., Routh P., Anno P. and Castagna J. 2005. Scale attributes from continuous wavelet transform. 75th SEG Meeting, Houston, USA, Expanded Abstracts, 779–781.
- Sniieder R. 1990. A perturbative analysis of nonlinear inversion. *Geophysical Journal International* **101**, 545–556.
- Zonge K.L. and Hughes L.J. 1991. Controlled source audio-frequency magnetotellurics. In: *Electromagnetic Methods in Applied Geophysics* (ed. M.N. Nabighian) Vol. 2, pp.713–809. Society of Exploration Geophysicists.

## APPENDIX A

In this appendix we present the necessary equations to represent the singular value decomposition of the inverse Hessian and the resolution matrices. Denoting  $\tilde{\mathbf{G}} = \mathbf{W}_d \mathbf{G}$  and assuming the model weighting matrix as diagonal, the inverse Hessian matrix is given by  $\mathbf{H}^{-1} = (\tilde{\mathbf{G}}^T \tilde{\mathbf{G}} + \beta \mathbf{I})^{-1}$  and the resolution matrix  $\mathbf{R} = (\tilde{\mathbf{G}}^T \tilde{\mathbf{G}} + \beta \mathbf{I})^{-1} \tilde{\mathbf{G}}^T \tilde{\mathbf{G}}$ . We denote  $\tilde{\boldsymbol{\varepsilon}} = \mathbf{W}_d \boldsymbol{\varepsilon}$  and decompose the matrix  $\tilde{\mathbf{G}} = \mathbf{U} \boldsymbol{\Lambda} \mathbf{V}^T$  using SVD. The expression for inverse Hessian can be obtained by solving  $\mathbf{H} \mathbf{x} = \mathbf{b}$  using SVD. The SVD representation of the equation  $(\tilde{\mathbf{G}}^T \tilde{\mathbf{G}} + \beta \mathbf{I}) \mathbf{x} = \mathbf{b}$  is given by  $(\mathbf{V} \boldsymbol{\Lambda}^2 \mathbf{V}^T + \beta \mathbf{I}) \mathbf{x} = \mathbf{b}$ . The estimated solution is given by  $\hat{\mathbf{x}} = \mathbf{V} \mathbf{V}^T \mathbf{x} = \mathbf{V} (\boldsymbol{\Lambda}^2 + \beta \mathbf{I})^{-1} \mathbf{V}^T \mathbf{b}$ . Thus we can denote the inverse Hessian by  $\mathbf{H}^{-1} = \mathbf{V} (\boldsymbol{\Lambda}^2 + \beta \mathbf{I})^{-1} \mathbf{V}^T$ . Therefore the difference in the inverse Hessian is given by

$$\mathbf{H}_2^{-1} - \mathbf{H}_1^{-1} = \mathbf{V} \left( \frac{1}{\boldsymbol{\Lambda}^2 + \beta_2} - \frac{1}{\boldsymbol{\Lambda}^2 + \beta_1} \right) \mathbf{V}^T. \quad (\text{A1})$$

To clarify the notation, the matrix inside the brackets in equation (A1) is a diagonal matrix such that  $1/\boldsymbol{\Lambda}^2 + \beta = \text{diag}(1/\boldsymbol{\Lambda}_1^2 + \beta, 1/\boldsymbol{\Lambda}_2^2 + \beta, \dots, 1/\boldsymbol{\Lambda}_M^2 + \beta)$ . In equation (A1) if we consider  $\boldsymbol{\Lambda} > (\beta_2, \beta_1)$ , the difference in singular spectrum is negligible. However, when  $\boldsymbol{\Lambda} \rightarrow 0$  the difference in the singular spectrum is not zero and therefore the difference in the inverse Hessian will not be zero. This insight into the inverse Hessian is useful; however for the noise term in equation (11), we are interested in the projection of the inverse Hessian on to the adjoint operator, i.e.  $\mathbf{H}^{-1} \tilde{\mathbf{G}}^T = (\tilde{\mathbf{G}}^T \tilde{\mathbf{G}} + \beta \mathbf{I})^{-1} \tilde{\mathbf{G}}^T$ . For example, the noise term is given by  $\mathbf{H}^{-1} \tilde{\mathbf{G}}^T \tilde{\boldsymbol{\varepsilon}} = (\tilde{\mathbf{G}}^T \tilde{\mathbf{G}} + \beta \mathbf{I})^{-1} \tilde{\mathbf{G}}^T \tilde{\boldsymbol{\varepsilon}}$ . Writing it using SVD, we obtain  $\mathbf{H}^{-1} \tilde{\mathbf{G}}^T \tilde{\boldsymbol{\varepsilon}} = \mathbf{V} (\boldsymbol{\Lambda}^2 / \boldsymbol{\Lambda}^2 + \beta) \mathbf{U}^T \tilde{\boldsymbol{\varepsilon}}$ . Thus the difference in the noise terms between the two inversions is given by

$$(\mathbf{H}_2^{-1} - \mathbf{H}_1^{-1}) \tilde{\mathbf{G}}^T \tilde{\boldsymbol{\varepsilon}} = \mathbf{V} \left( \frac{\boldsymbol{\Lambda}}{\boldsymbol{\Lambda}^2 + \beta_2} - \frac{\boldsymbol{\Lambda}}{\boldsymbol{\Lambda}^2 + \beta_1} \right) \mathbf{U}^T \tilde{\boldsymbol{\varepsilon}}. \quad (\text{A2})$$

To obtain the expression for the resolution matrix, we solve  $(\tilde{\mathbf{G}}^T \tilde{\mathbf{G}} + \beta \mathbf{I}) \mathbf{x} = \tilde{\mathbf{G}}^T \tilde{\mathbf{G}} \mathbf{b}$  using SVD. The resulting solution is given by  $\hat{\mathbf{x}} = \mathbf{V} \mathbf{V}^T \mathbf{x} = \mathbf{V} (\boldsymbol{\Lambda}^2 / \boldsymbol{\Lambda}^2 + \beta)^{-1} \mathbf{V}^T \mathbf{b}$ , such that we can represent the resolution matrix as  $\mathbf{R} = \mathbf{V} (\boldsymbol{\Lambda}^2 / \boldsymbol{\Lambda}^2 + \beta)^{-1} \mathbf{V}^T$ . Thus the difference in the resolution matrix  $\mathbf{R}_2 - \mathbf{R}_1$  is given by

$$\mathbf{R}_2 - \mathbf{R}_1 = \mathbf{V} \left( \frac{\boldsymbol{\Lambda}^2}{\boldsymbol{\Lambda}^2 + \beta_2} - \frac{\boldsymbol{\Lambda}^2}{\boldsymbol{\Lambda}^2 + \beta_1} \right) \mathbf{V}^T. \quad (\text{A3})$$

## APPENDIX B

In this section we derive the relationship between the region of data influence and the resolution matrix when the model weighting matrix is more general than diagonal weighting. Although the derivation using the SVD for diagonal model weighting is insightful, in reality the prior information used in inverse problems is often far more complicated than a diagonal operator. The region of data influence (RDI) in equation (7) can be considered as an approximation of the derivative which can be stated as: determine the change in the inverted model given a change in the reference model. This allows us to write

$$RDI = \left| \frac{\delta \hat{\mathbf{m}}}{\delta \mathbf{m}_0} \right|, \quad (\text{B1})$$

where  $\delta \mathbf{m}_0$  is the perturbation in the reference model that results in the perturbation of the inverted model  $\delta \hat{\mathbf{m}}$ . To proceed further, we consider equation (8) and write it in an expanded form, given by

$$\hat{\mathbf{m}} = \mathbf{m}_0 + \left( \tilde{\mathbf{G}}^T \tilde{\mathbf{G}} + \beta \mathbf{W}_m^T \mathbf{W}_m \right)^{-1} \tilde{\mathbf{G}}^T \tilde{\mathbf{G}} (\mathbf{m} - \mathbf{m}_0) + \left( \tilde{\mathbf{G}}^T \tilde{\mathbf{G}} + \beta \mathbf{W}_m^T \mathbf{W}_m \right)^{-1} \tilde{\mathbf{G}}^T \tilde{\boldsymbol{\varepsilon}}. \quad (\text{B2})$$

Next we perturb the reference model  $\mathbf{m}_0 \rightarrow \mathbf{m}_0 + \delta \mathbf{m}_0$ . This results in the perturbation of the regularization parameter  $\beta \rightarrow \beta + \delta \beta$  and consequently it changes the inverted model from  $\hat{\mathbf{m}} \rightarrow \hat{\mathbf{m}} + \delta \hat{\mathbf{m}}$ . Mathematically this can be represented by

$$\hat{\mathbf{m}} + \delta \hat{\mathbf{m}} = \mathbf{m}_0 + \delta \mathbf{m}_0 + \left( \tilde{\mathbf{G}}^T \tilde{\mathbf{G}} + (\beta + \delta \beta) \mathbf{W}_m^T \mathbf{W}_m \right)^{-1} \times \tilde{\mathbf{G}}^T \tilde{\mathbf{G}} (\mathbf{m} - \mathbf{m}_0 - \delta \mathbf{m}_0) + \left( \tilde{\mathbf{G}}^T \tilde{\mathbf{G}} + (\beta + \delta \beta) \mathbf{W}_m^T \mathbf{W}_m \right)^{-1} \tilde{\mathbf{G}}^T \tilde{\boldsymbol{\varepsilon}}. \quad (\text{B3})$$

In a more compact notation, we can write equation (B3) as

$$\hat{\mathbf{m}} + \delta \hat{\mathbf{m}} = \mathbf{m}_0 + \delta \mathbf{m}_0 + (\mathbf{H} + \delta \mathbf{H})^{-1} \tilde{\mathbf{G}}^T \tilde{\mathbf{G}} \times (\mathbf{m} - \mathbf{m}_0 - \delta \mathbf{m}_0) + (\mathbf{H} + \delta \mathbf{H})^{-1} \tilde{\mathbf{G}}^T \tilde{\boldsymbol{\varepsilon}}, \quad (\text{B4})$$

where  $\mathbf{H} = (\tilde{\mathbf{G}}^T \tilde{\mathbf{G}} + \beta \mathbf{W}_m^T \mathbf{W}_m)$  and  $\delta \mathbf{H} = \delta \beta \mathbf{W}_m^T \mathbf{W}_m$ . The inverse Hessian operation in equation (B4) can be written as  $(\mathbf{H} + \delta \mathbf{H})\mathbf{x} = \mathbf{b}$ . The solution is given by  $\mathbf{x} = (\mathbf{I} + \mathbf{H}^{-1} \delta \mathbf{H})^{-1} \mathbf{H}^{-1} \mathbf{b}$ . To first order the solution can be written as  $\mathbf{x} \approx (\mathbf{I} - \mathbf{H}^{-1} \delta \mathbf{H}) \mathbf{H}^{-1} \mathbf{b} = \mathbf{H}^{-1} \mathbf{b} - \mathbf{H}^{-1} \delta \mathbf{H} \mathbf{H}^{-1} \mathbf{b}$  by neglecting the higher-order terms in the series expansion. Applying this expression to equation (B4), we obtain

$$\begin{aligned} \hat{\mathbf{m}} + \delta \hat{\mathbf{m}} &= \mathbf{m}_0 + \delta \mathbf{m}_0 + \mathbf{H}^{-1} \tilde{\mathbf{G}}^T \tilde{\mathbf{G}} (\mathbf{m} - \mathbf{m}_0 - \delta \mathbf{m}_0) \\ &\quad - \mathbf{H}^{-1} \delta \mathbf{H} \mathbf{H}^{-1} \tilde{\mathbf{G}}^T \tilde{\mathbf{G}} (\mathbf{m} - \mathbf{m}_0 - \delta \mathbf{m}_0) \\ &\quad + \mathbf{H}^{-1} \tilde{\mathbf{G}}^T \tilde{\boldsymbol{\varepsilon}} - \mathbf{H}^{-1} \delta \mathbf{H} \mathbf{H}^{-1} \tilde{\mathbf{G}}^T \tilde{\boldsymbol{\varepsilon}}. \end{aligned} \quad (\text{B5})$$

By rearranging terms, writing  $\mathbf{R} = \mathbf{H}^{-1} \tilde{\mathbf{G}}^T \tilde{\mathbf{G}}$  and substituting  $\delta \mathbf{H} = \delta \beta \mathbf{W}_m^T \mathbf{W}_m$ , we obtain

$$\begin{aligned} \hat{\mathbf{m}} + \delta \hat{\mathbf{m}} &= (\mathbf{m}_0 + \mathbf{R} (\mathbf{m} - \mathbf{m}_0) + \mathbf{H}^{-1} \tilde{\mathbf{G}}^T \tilde{\boldsymbol{\varepsilon}}) + (\delta \mathbf{m}_0 - \mathbf{R} \delta \mathbf{m}_0) \\ &\quad - \delta \beta \mathbf{H}^{-1} \mathbf{W}_m^T \mathbf{W}_m \mathbf{R} (\mathbf{m} - \mathbf{m}_0 - \delta \mathbf{m}_0) \\ &\quad - \delta \beta \mathbf{H}^{-1} \mathbf{W}_m^T \mathbf{W}_m \mathbf{H}^{-1} \tilde{\mathbf{G}}^T \tilde{\boldsymbol{\varepsilon}}. \end{aligned} \quad (\text{B6})$$

Using equation (B2), equation (B6) can be simplified to obtain

an expression in terms of the inverted model perturbation, given by

$$\begin{aligned} \delta \hat{\mathbf{m}} &= (\mathbf{I} - \mathbf{R}) \delta \mathbf{m}_0 - \delta \beta \mathbf{H}^{-1} \mathbf{W}_m^T \mathbf{W}_m \\ &\quad \times (\mathbf{R} (\mathbf{m} - \mathbf{m}_0 - \delta \mathbf{m}_0) + \mathbf{H}^{-1} \tilde{\mathbf{G}}^T \tilde{\boldsymbol{\varepsilon}}). \end{aligned} \quad (\text{B7})$$

We can write  $\delta \beta \mathbf{H}^{-1} \mathbf{W}_m^T \mathbf{W}_m = (\delta \beta / \beta) \mathbf{H}^{-1} \beta \mathbf{W}_m^T \mathbf{W}_m = (\delta \beta / \beta) (\mathbf{I} - \mathbf{R})$ . Thus equation (B7) can be further simplified into the form,

$$\delta \hat{\mathbf{m}} = (\mathbf{I} - \mathbf{R}) \left( \delta \mathbf{m}_0 - \frac{\delta \beta}{\beta} (\mathbf{R} (\mathbf{m} - \mathbf{m}_0 - \delta \mathbf{m}_0) + \mathbf{H}^{-1} \tilde{\mathbf{G}}^T \tilde{\boldsymbol{\varepsilon}}) \right). \quad (\text{B8})$$

If the ratio  $(\delta \beta / \beta)$  in equation (B8) is small, then we obtain the following relationship,

$$\delta \hat{\mathbf{m}} \approx (\mathbf{I} - \mathbf{R}) \delta \mathbf{m}_0. \quad (\text{B9})$$

Thus for a general model weighting matrix we also observe that the approximate relationship between the region of data influence and the resolution matrix is the same as that obtained in equation (22).